JMEPEG (2008) 17:831–837
DOI: 10.1007/s11665-008-9246-0

1059-9495/$19.00

Modeling and Experimental Validation of Ductile Iron Castings During Solidification

Jianzheng Guo and Mark T. Samonds

(Submitted September 17, 2007; in revised form March 28, 2008)

Ductile irons are still important engineering materials due to their high strength and toughness, and relatively low price. In the foundries, ductile irons suffer from shrinkage porosity formation during solidification, which is detrimental to the mechanical properties. In order to minimize porosity formation, large risers are normally used in the design, which reduces porosity level sometimes but leads to a low yield. In order to better understand the shrinkage behavior of ductile iron during solidification, a micro model was developed to simulate the microstructure formation. The density change during solidification and the room temperature mechanical properties can be calculated based on the microstructure. The simulation has been compared with the experimental results and found to be in good agreement.

Keywords cast irons, casting, modeling processes

1. Introduction

Cast iron remains the most important casting material with over 70% of the total world tonnage (Ref 1). Based on the shape of graphite, cast iron can be lamellar (flake) graphite iron or spheroidal (nodular) graphite iron. In the last 40 years, many papers have been published on the modeling of ductile iron solidification. It started with the computational modeling by analytical heat transport and transformation kinetics calculations (Ref 2-8). The computer model can calculate the cooling curve with an analytical method, together with the kinetics calculation of carbon diffusion through the gamma phase shell. In 1985, Su et al. (Ref 9) first coupled heat transfer and solidification kinetics in a model using the finite difference method. After that, many papers have been published on micro modeling of ductile iron solidification (Ref 10-20). The carbon diffusion controlled growth through the gamma shell was treated. In those models, the nodule count, graphite radius, and austenite shell radius were calculated. Onsoien et al. (Ref 21-22) used the internal state variable approach to model the multiple phase changes occurring during solidification and subsequent cooling of near eutectic ductile cast iron. In their simulation, the effects on the microstructure evolution at various stages of the process due to alloy composition, graphite nucleation potential, and thermal progress were illuminated. The heat flow, fading effect, graphite/austenite eutectic transformation, ledeburite eutectic transformation, graphite growth in the austenite regime, and the eutectoid transformation were all modeled. There is one common assumption for all the models mentioned above. The thermo-physical properties, such as thermal conductivity and density, are constants. It is well known that density as well as thermal conductivity is strongly composition, temperature, and process dependent. Shrinkage porosity can form because of the density variation during solidification. For ductile iron, expansion can happen during solidification because of the graphite precipitation based on the composition, inoculation, and other processes.

The microstructure has been extensively studied so far but not the porosity formation because of the density variation of ductile cast iron during solidification. Chen et al. (Ref 20) calculated the densities of austenite, graphite, and liquid and the volume change as well as coupling the volume change model to the growth kinetic model. In their model the density of ledeburite phase was not included. Ledeburite phase can form when cooling is too fast or the inoculation is not good enough. In their model, the density calculation was not coupled to the porosity prediction.

In this article, a comprehensive micro model is developed which can give accurate microstructure information as well as the mechanical properties, such as yield strength, tensile strength, and hardness. The density of austenite, ferrite, pearlite, graphite, liquid, and ledeburite are all calculated. The prediction has been compared with the experimental results and found to be in good agreement.

Jianzheng Guo, GE Global Research Center, One Research Circle, Niskayuna, NY 12309; and **Mark T. Samonds**, ESI US R&D, 6851 Oak Hall Lane, Ste 119, Columbia, MD 21045. Contact e-mail: jianzhengguo@gmail.com.

2. Micro Modeling

2.1 Nucleation Model

In this work, Oldfield's nucleation model is applied. Bulk heterogeneous nucleation occurs at foreign sites which are already present within melt or intentionally added to the melt by inoculation.

$$N_o = A(\Delta T)^n \quad \text{(Eq 1)}$$

where A is the nucleation constant, N_o is the nucleation number per unit volume, ΔT is the undercooling, and n is another constant which depends on the effectiveness of inoculation.

2.2 Fading Effect

Fading is the phenomenon whereby the effectiveness of inoculation diminishes as the time between inoculation and casting increases. It is believed that the nucleation of graphite occurs on small nonmetallic inclusions which are entrapped in the liquid after the inoculation (Ref 21). The small particles will grow with time. The particle diameter can be calculated by:

$$d = (d_o^3 + kt)^{1/3} \quad \text{(Eq 2)}$$

where d is the particle diameter with time, d_o is the particle diameter at the beginning of inoculation, and k is a kinetic constant.

2.3 Graphite/Austenite Eutectic Transformation

The eutectic growth process in ductile iron is a divorced growth of austenite and graphite, which do not grow concomitantly. At the beginning of the liquid/solid transformation, graphite nodules nucleate in the liquid and grow in the liquid to a small extent. The formation of graphite nodules and their limited growth in liquid depletes the carbon in the melt in the vicinity of the nodules. This facilitates the nucleation of austenite around the nodules, forming a shell. Further growth of these nodules is by diffusion of carbon from the melt through the austenitic shell. Once the austenite shell is formed around each nodule, the diffusion equation for carbon through the austenitic shell is solved in 1D spherical coordinates. The boundary conditions are known from the phase diagram because thermodynamic equilibrium is maintained locally. Conservation of mass and solute is maintained in each grain. Because of the density variation resulting from the growth of austenite and graphite, the expansion/contraction of the grain is taken into account by allowing the final grain size to vary. Toward the end of solidification, the grains impinge on each other. This is taken into consideration by using the Johnson-Mehl approximation.

Using spherical coordinates, a mass balance is written as:

$$\rho_G \frac{4}{3}\pi R_G^3 + \rho_\gamma \frac{4}{3}\pi (R_\gamma^3 - R_G^3) + \rho_l \frac{4}{3}\pi (R_l^3 - R_\gamma^3) = m_{av} \quad \text{(Eq 3)}$$

where ρ_G, ρ_γ, ρ_l are the densities of graphite, austenite, and liquid respectively and the calculation can be found in the next section; R_G, R_γ, R_l are radii of graphite, austenite, and the final grain respectively; m_{av} is average mass of the grain. It is recommended to read the descriptive figure (Fig. 5 in (Ref 16)) for better understanding the above equation.

Assuming complete mixing of solute in liquid, the overall solute balance is written as:

$$\rho_G \cdot 1 \cdot \frac{4}{3}\pi R_G^3 + \int_{R_c}^{R_a} \rho_\gamma c(r,t) 4\pi r^2 dr + \rho_l c_l \frac{4}{3}\pi (R_l^3 - R_\gamma^3) = c_{av} \quad \text{(Eq 4)}$$

Differentiation of the above two equations and using Fick's law in spherical coordinates leads to two equations for graphite and austenite growth rates following some manipulation.

2.4 Ledeburite Eutectic Transformation

When the temperature reaches below the metastable eutectic temperature, the metastable phase forms. The metastable cementite eutectic is also called ledeburite, in which small islands of austenite are dispersed in the carbide phase. It has both direct and indirect effects on the properties of ductile iron castings. It increases the yield strength but reduces the tensile strength with an increasing volume percent of the hard, brittle carbide. Following the assumptions from Onsoien (Ref 22), the graphite/austenite nodule distribution is approximated by that of a close-packed face-centered space lattice and the ledeburite eutectic appears in intermediate positions. The total number of ledeburite nucleation sites is the same as graphite/austenite nodules. The grain is assumed to be spherical. Hence the growth of the ledeburite can be calculated as:

$$\frac{dR_{LE}}{dt} = 30.0 \times 10^{-6} * (\Delta T)^n \quad \text{(Eq 5)}$$

So the fraction of ledeburite can be written as:

$$f_{LE} = \frac{4}{3}\pi N R_{LE}^3 \quad \text{(Eq 6)}$$

where N is the nodule count.

2.5 Eutectoid Transformation

The eutectoid reaction leads to the decomposition of austenite to ferrite and graphite for the case of the stable eutectoid, and to pearlite for the metastable eutectoid transformation. Usually, the metastable eutectoid temperature is lower than the stable eutectoid temperature. Slower cooling rates result in more stable eutectoid structure. Following solidification, the solubility of carbon in austenite decreases with the drop in temperature until the stable eutectoid temperature is reached. The rejected carbon migrates toward the graphite nodules, which are the carbon sinks. This results in carbon depleted regions in austenite around the graphite nodules. This provides favorable sites for ferrites to nucleate, which grow as a shell around the graphite nodules. If the complete transformation of austenite is not achieved when the metastable temperature is reached, pearlite forms and grows in competition with ferrite.

2.5.1 Growth of Ferrite. Even though ferrite can form either from the breakdown of pearlite or from the direct decomposition of austenite, it is assumed here that ferrite results from the latter source only. It is assumed that (1) the austenite to ferrite transformation occurs at steady state and is controlled by carbon diffusion, (2) thermodynamic equilibrium exists at graphite/ferrite and ferrite/austenite interface, and (3) diffusion from the ferrite/austenite interface toward austenite is neglected as diffusion coefficients and concentration gradients in austenite are small compared to those in ferrite.

Solution of the diffusion equation of carbon in ferrite with the flux balance at the ferrite/austenite interface leads to the following equation:

$$\frac{dR_F}{dt} = \frac{\rho_\gamma}{\rho_F} D_c^F \frac{R_G}{R_F(R_F - R_G)} \frac{C^{\gamma F} - C^{GF}}{C^{F\gamma} - C^{\gamma F}} \quad \text{(Eq 7)}$$

where D_c^F is the carbon diffusion coefficient in ferrite, R_F is the radius of the ferrite grain, and C^{GF}, $C^{F\gamma}$, $C^{\gamma F}$ are the carbon concentration in ferrite at the graphite/ferrite, ferrite/austenite, and carbon concentration in austenite at the ferrite/austenite interface respectively.

Since the rejected carbon migrates to the graphite nodule, concomitant growth of ferrite and graphite results the following equation from mass conservation:

$$\rho_G \frac{4}{3}\pi[(R_G + dR_G)^3 - R_G^3]C_G = \rho_F \frac{4}{3}\pi[(R_F + dR_F)^3 - R_F^3]C^{\gamma F} \quad \text{(Eq 8)}$$

Therefore, knowing the radius of the ferrite grain, the radius of the graphite nodule can be obtained from the above equation. Then the change rate of fraction of ferrite grain is obtained by:

$$\frac{df_F}{dt} = (1 - f_F - f_P)4\pi N R_F^2 \frac{dR_F}{dt} \quad \text{(Eq 9)}$$

where f_F, f_P are fractions of ferrite and pearlite, N is nodule count.

2.5.2 Nucleation and Growth of Pearlite. The nucleation of pearlite usually occurs at austenite grain boundaries. It has been demonstrated that pearlite colonies grow either as spheres or hemispheres following nucleation. By the movement of high mobility incoherent interfaces, these colonies can grow edgewise or sidewise into the austenite. This means that pearlite grows in competition with ferrite until austenite is completely transformed. Transformation of austenite into pearlite is usually modeled with an Avrami equation because the study of nucleation of pearlite is difficult, especially under continuous cooling conditions. Also, pearlite grains impinge on each other at an early stage, especially at a relatively high cooling rate. Here, equations for nucleation and growth of pearlite grains can be written as:

$$\frac{dN_p}{dt} = 5.07 \times 10^6 \exp\left(-\frac{370}{\Delta T_{eud}}\right) \quad \text{(Eq 10)}$$

$$\frac{dR_p}{dt} = 0.0168 \exp\left(-\frac{94.8}{\Delta T_{eud}}\right) [\text{cm/s}] \quad \text{(Eq 11)}$$

where the pearlite nucleation density is given in nuclei/mm^3/s and the undercooling is given in K. The nucleation process stops once the minimum in the cooling curve is reached. The expression for the time rate of change of fraction of pearlite transformed is given by an expression similar to that for ferrite.

3. Density Calculation

Thermo-physical properties research is a very important part of materials science, particularly at the current times because such data are a critical input for the simulation of metals processing. There is little information about such properties for multicomponent alloys during solidification. A simple pairwise mixture model, which is similar to that used to model thermodynamic excess functions in multi-component alloys, is used to calculate the properties (Ref 23).

$$P = \sum x_i P_i + \sum_i \sum_{j>i} x_i x_j \sum_v \Omega_v (x_i - x_j)^v \quad \text{(Eq 12)}$$

where P is the phase property, P_i is the property of the pure element in the phase, Ω_i is a binary interaction parameter, and x_i and x_j are the mole fractions of elements i and j in that phase.

A database has been developed containing molar volume and thermal volume coefficients of expansion of liquid, solid solution elements, and graphite for ductile iron castings. The densities of the liquid, solid, and graphite phases of multicomponent systems are calculated by the simple mixture model (Ref 24, 25). The expansion phenomena can be well detected if the microstructure is predicted accurately.

4. Mechanical Properties Calculation

The ultimate goal of process modeling is to predict the final mechanical properties. The mechanical properties (hardness, tensile strength, yield strength, and elongation) of ductile iron castings are function of composition and microstructure. The graphite shape, graphite structure, graphite amount, carbide content, and matrix structure (pearlite, ferrite) all affect the mechanical properties of ductile iron castings. Carbide content has direct and indirect effects on the properties of cast ductile irons. The hard brittle carbide increases the yield strength but decreases the tensile strength. As for the matrix structure, the increasing of pearlite amount increases the strength and hardness but reduces the elongation. Mixture rule is applied here to calculate the mechanical properties. For example, the hardness can be calculated by:

$$HB = \sum_{i=1}^{n} HB_i f_i \quad \text{(Eq 13)}$$

where i is phase number, n is total number of phase, $HB_i = f(d)$ is the hardness of phase i and is a function of grain size, f_i is volume fraction of phase i.

5. Case Studies

In order to show the capability of this model, solidification of a simple geometry ductile iron casting was investigated. The dimension of the casting is $10 \times 10 \times 200$ cm and the geometry of the casting is shown in Fig. 1. On the left face, it is cooled by contacting a constant temperature media (15 °C) with a heat transfer coefficient of 500 W/m^2 K. All the other faces are adiabatic. The initial melt temperature is 1400 °C. Figure 2 shows the solidification time at different distances from the cooling end. At the very left, the solidification time is less than 1 s. On the other hand, the solidification time at 10 cm from the cooling end is more than 100 s. Because of the different cooling rates, the nodule count varies and is shown in the same figure. The metastable phase forms when the cooling is too fast.

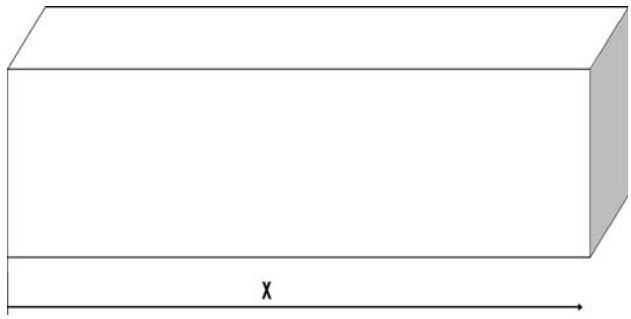

Fig. 1 Geometry for a test casting to show the ability of current model

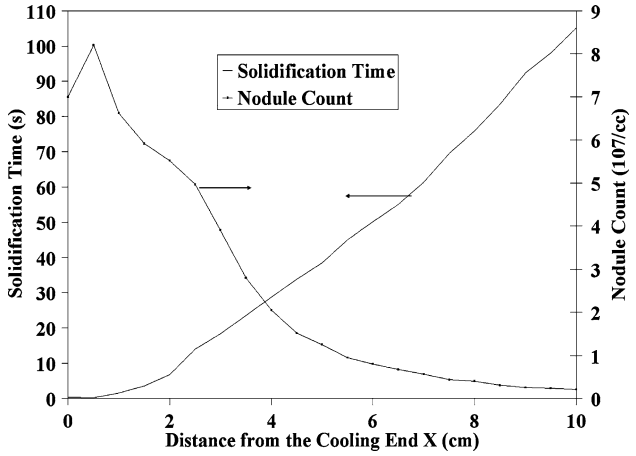

Fig. 2 The relationship between solidification time and nodule count due to the different solidification rates at different distances from the chill

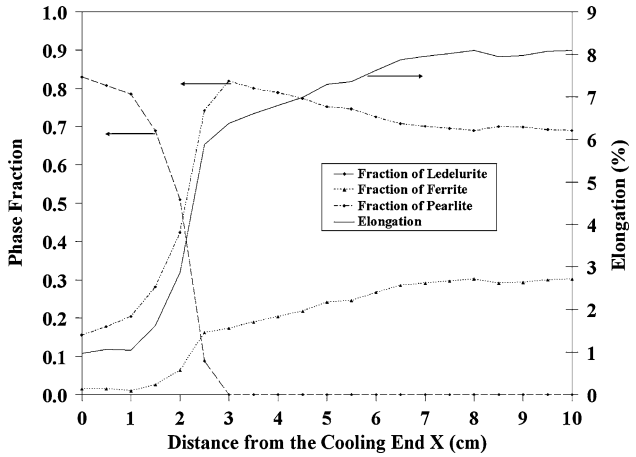

Fig. 3 The relationship between phase fractions and the elongation of the casting at different distances from the chill

Figure 3 shows the volume fraction of different phases at room temperature. On the very left end, there is around 90% volume fraction of metastable phase ledeburite thanks to the rapid cooling. The ledeburite phase reduces gradually from left to right until at 3 cm from the chill end, there is no more ledeburite. At the same time, as cooling decreases, the volume fraction of ferrite increases and that of pealite decreases. Ledeburite is a very hard, brittle phase, harder than pearlite. The pearlite phase is harder than ferrite. Hence the ductility increases as the cooling rate decreases. From the micro modeling, the calculated grain and graphite radius at different distances from the chill are shown in Fig. 4. Faster cooling results in smaller grain and graphite sizes. The ratio of the radius of graphite and austenite increases as cooling decreases, but reaches a constant value of around 0.46 even though the radius of graphite and austenite still continue to increase. This constant ratio is determined by the initial carbon content. It can determine the expansion level during solidification.

Based on the microstructure, the mechanical properties can be calculated. As mentioned above, carbide increases the yield strength but decreases the tensile strength. The yield strength

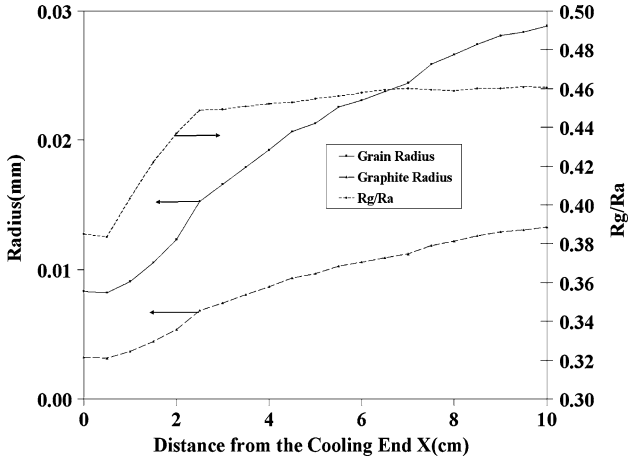

Fig. 4 The relationship between the grain and graphite size of the casting because of the different cooling conditions at different distances from the chill

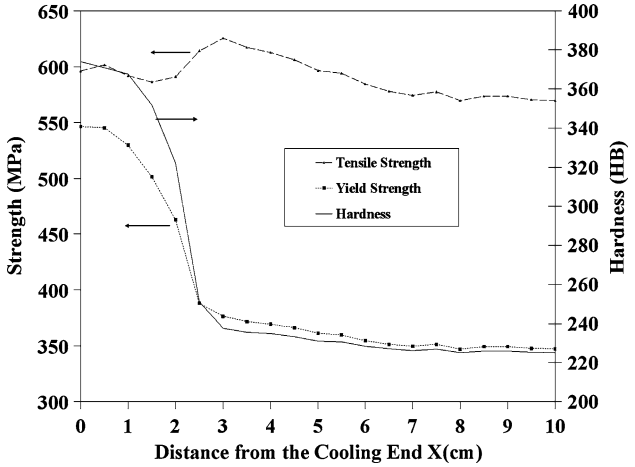

Fig. 5 Mechanical properties of the casting at different distances from the chill

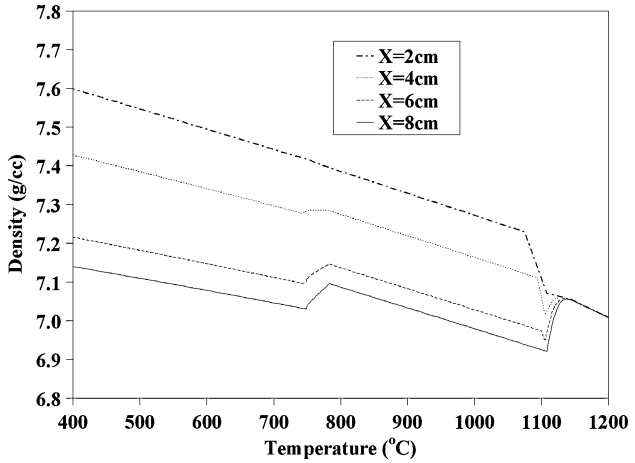

Fig. 6 Density variations of the casting at different distances from the chill

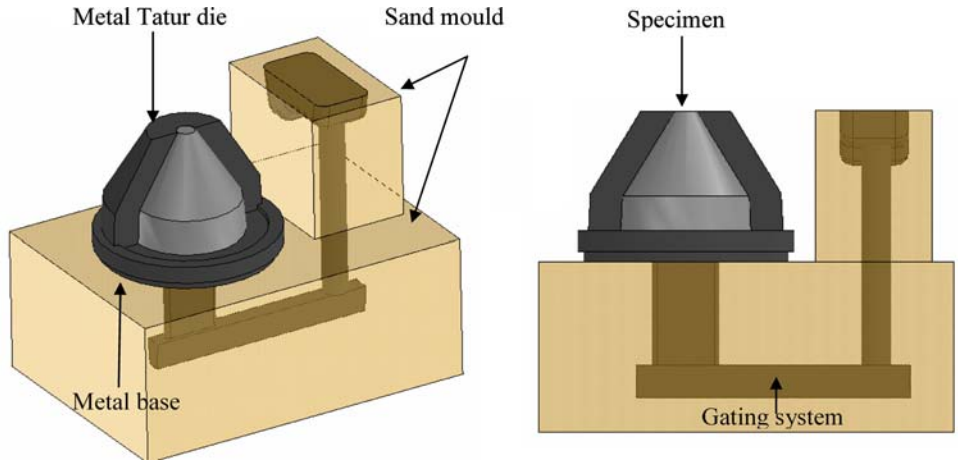

Fig. 7 Experiment setup

and hardness continuously decrease as the cooling rate decreases. The yield strength is very high on the left because of the formation of carbide. The results are shown in Fig. 5.

Based on the volume fraction of different phases and the composition, the density variation with temperature can be predicted and is shown in Fig. 6. It can be seen that at $x = 0$, because of the formation of carbide, there is no expansion during solidification. The density continuously increases as temperature decreases. Dependent on the locations from the cooling end, the expansion levels are different based on the microstructure at that location. There is a secondary expansion during eutectoid reaction around 1000 K because of the phase transformation of austenite to ferrite and/or pearlite phase. The density variation for the liquid stage is the same at different location because the initial composition is uniform and macrosegregation is not included in this model. Different cooling will cause different solid density profile even with the same initial chemistry because of the different microstructure. As a result, the porosity can be predicted accurately.

6. Experimental Validations

In order to validate the model, a series of experiments were performed (Ref 26). The three-part cast-iron foundry mould containing the gating system is shown in Fig. 7. The casting is GGG60 ductile iron. The pouring temperature is 1400 °C, the initial die temperature is 165 °C, and the initial sand temperature is 20 °C. Table 1 shows the chemistry of the casting.

In order to investigate the micro structure of the casting and the morphology of the graphite, specimens were taken as shown in Fig. 8. The specimens were then grounded, polished, and etched for structure evaluation. It can be seen in the pictures of the microstructure that graphite was segregated in the form of spheroids.

Because of the rapid cooling, a large amount of the metastable phase, ledeburite, was formed in the corners. The ledeburite phase reduces gradually as the cooling rate decreases. In the center of the casting, no ledeburite phase was found. The radius of the black graphite balls increases as cooling decreases. The structure of the metal is formed with pearlite and ferrite. Figure 9 shows the volume fraction of

Table 1 Chemical composition

C, %	Mn, %	Si, %	P, %	S, %	Cr, %	Ni, %	Cu, %
3.63	0.68	2.38	0.043	0.005	0.02	0.01	0.02

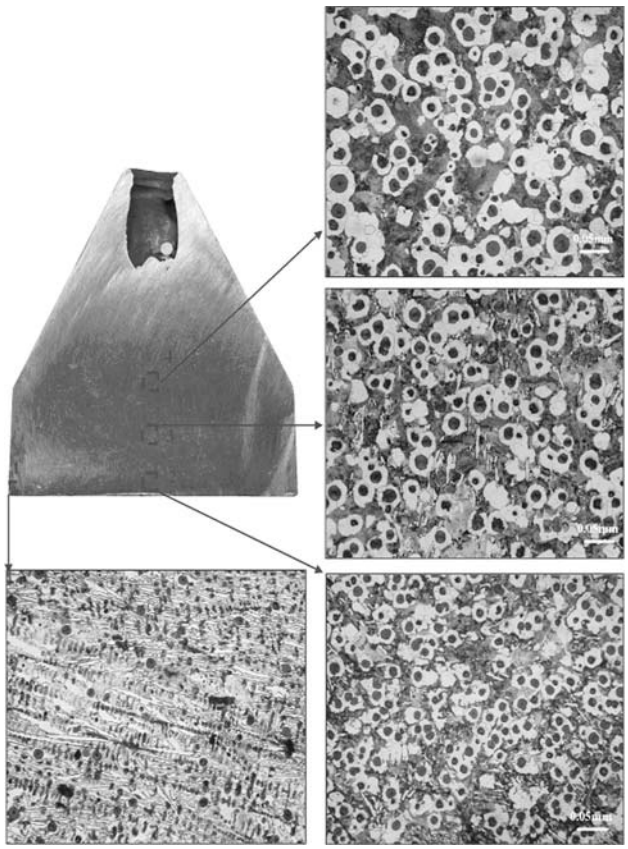

Fig. 8 Microstructure of the ductile iron casting at indicated locations

metastable phase (Fig. 9a) and volume fraction of ferrite (Fig. 9b). It is difficult to measure the yield strength of the sample at different location because the strength could change

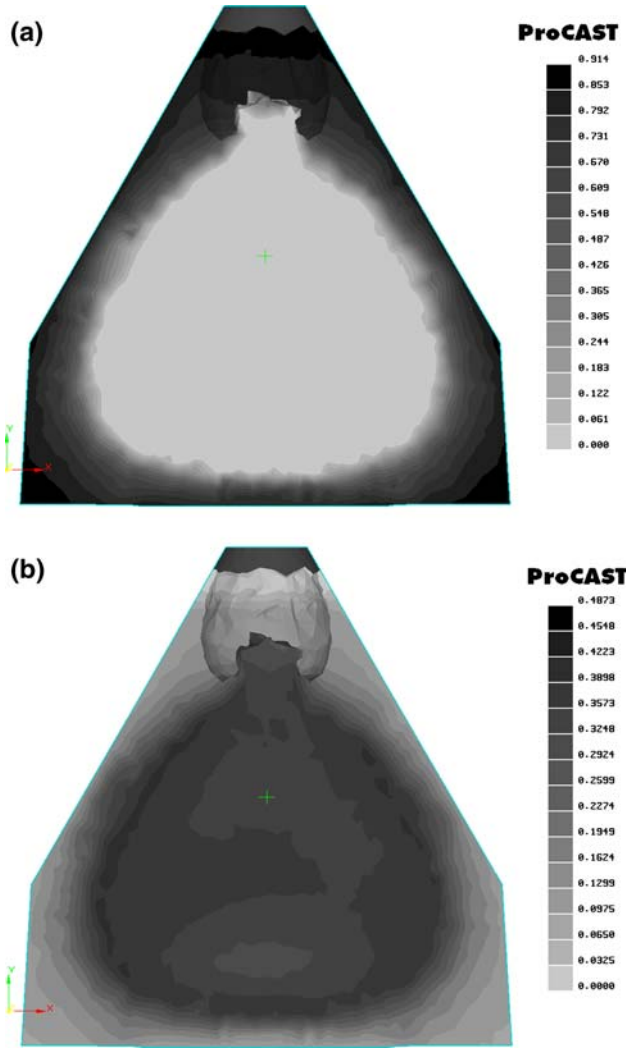

Fig. 9 (a) Predicted fraction of metastable phase and (b) predicted fraction of ferrite

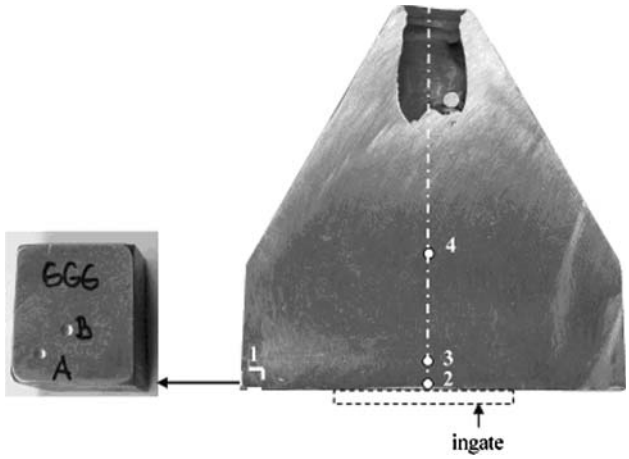

Fig. 10 Experimental sample for hardness measurement

dramatically based on the microstructure variation. On the other hand, hardness is an excellent indicator of microstructure and strength and relatively easy to measure. Figure 10 shows the hardness measurement points on the sample. Table 2 shows the comparison between the measurement and prediction results of the hardness at different locations. It can be concluded that the prediction matches the experiments very well.

Table 2 Comparison between measured and predicted hardness

Location	Dimension *x*, mm	Dimension *y*, mm	Measurement HB	Simulated HB
1 A	4	4	368	371
1 B	10	7	313	320
2	50	4	249	255
3	50	10	236	245
4	50	48	209	203

7. Conclusions

A micro model was developed to simulate the microstructure formation of ductile iron. Based on the microstructure, the volume fraction of different phases, and the composition, the density variation with temperature can be predicted. Dependent on the cooling condition, the expansion levels are different because of the different microstructure at that location. Hence, different cooling will cause different solid density profile even with the same initial chemistry. As a result, the porosity can be predicted accurately. Based on the microstructure, the mechanical properties can be calculated as well. The simulation, such as hardness, has been compared with the experimental results and found to be in good agreement. Further microstructure prediction validation, such as graphite nodule size and nodule count, will be performed next.

References

1. D.M. Stefanescu, Solidification and Modeling of Cast Iron—A Short History of the Defining Moments, *Mater. Sci. Eng. A*, 2005, **V413–414**, p 322–333
2. W. Oldfield, A Qualitative Approach to Casting Solidification, *ASM Trans.*, 1966, **59**, p 945
3. D.M. Stefanescu and S. Trufinescu, Kinetics of Solidification of Gray Iron, *Z. Metall.*, 1974, **9**, p 610
4. H. Fredriksson and L. Svensson, Computer Simulation of Structure Formation and Segregation During the Solidification of Cast Iron, *The Physical Metallurgy of Cast Iron*, H. Fredriksson and M. Hillert, Eds., Elsevier, 1985, p 273–284
5. H. Fredriksson and L. Svensson, Simulation of Grey Cast-Iron Solidification in a Shaped Casting, *Solidification Processing of Eutectic Alloys*, D.M. Stefanescu, G.J. Abbaschian, and R.J. Bayuzick, Eds., The Metallurgical Soc., Warrendale, PA, 1988, p 153–162
6. D.M. Stefanescu and C. Kanetkar, Computer Modeling of the Solidification of Eutectic Alloys: The Case of Cast Iron, *Computer Simulation of Microstructural Evolution*, D.J. Srolovitz, Ed., The Metallurgical Soc., Warrendale, PA, 1985, p 171–188
7. J. Lacaze, M. Castro, C. Selig, and G. Lesoult, Solidification of Spheroidal Graphite Cast Irons, *Modeling of Casting, Welding and Advanced Solidification Processes V*, M. Rappaz, Ed., The Metallurgical Soc., Warrendale, PA, 1991, p 473–478
8. E. Fras, W. Kapturkiewicz, and A.A. Burbielko, Micro-Macro Modeling of Casting Solidification Controlled By Transient Diffusion and Undercooling, *Modeling of Casting, Welding and Advanced*

Solidification Processes VII, M. Croos, and J. Campbell, Eds., The Metallurgical Soc., Warrendale, PA, 1995, p 679–686
9. K.C. Su, I. Ohnaka, I. Yamauchhi, and T. Fukusako, Modelling of Solidified Structure of Castings, *The Physical Metallurgy of Cast Iron*, H. Fredriksson and M. Hillert, Eds., Elsevier, 1985, p 181–189
10. S. Chang, D. Shangguan, and D.M. Stefanescu, Prediction of Microstructural Evolution in SG Cast Iron from Solidification to Room Temperature, *Metall. Trans. A*, 1991, **22**, p 915
11. D.M. Stefanescu and C.S. Kanetkar, Computer Modeling of the Solidification of Eutectic Alloys: Comparison of Various Models for Eutectic Growth of Cast Iron, *AFS Trans*., 1987, p 139–144
12. L. Nastac and D.M. Stefanescu, Prediction of Gray-to-White Transition in Cast Iron by Solidification Modeling, *AFS Trans.*, 1995, **103**, p 329–337
13. D.M. Stefanescu, A. Catalina, X. Guo, L. Chuzhoy, M.A. Pershing, and G. L. Biltgen, *Solidification Processing 1997*, J. Beech and H. Jones, Eds., University of Sheffield, UK, 7–9 July 1997, p 609–613
14. G. Lesoult, M. Castro, and J. Lacaze, Solidification of Spheroidal Graphite Cast Irons—I. Physical Modelling, *Acta Mater.*, 1998, **46**(3), p 983–995
15. G. Lesoult, M. Castro, and J. Lacaze, Solidification of Spheroidal Graphite Cast Irons—II. Numerical Simulation, *Acta Mater.*, 1998, **46**(3), p 997–1010
16. F.J. Bradley, A Stereological Formulation for the Source Term in Micromodels of Equiaxed Eutectic Solidification, *Metall. Trans. B*, 1990, **24**, p 539
17. R. Vijayaraghavan and F.J. Bradley, Micro-Model for Eutectoid Phase Transformations in As-Cast Ductile Iron, *Scr. Mater.*, 1999, **41**(11), p 1247–1253
18. D. Venugopalan, Prediction of Matrix Microstructure in Ductile Iron, *Metall. Trans. A*, 1990, **21**, p 913–918
19. L. Nastac and D.M. Stefanescu, Prediction of Gray-to-White Transition in Cast Iron by Solidification Modeling, *AFS Trans.*, 1995, **103**, p 329–337
20. Q. Chen, E.W. Langer, and P.N. Hansen, Comparative Study on Kinetic Models and their Effects on Volume Change During Eutectic Reaction of S.G. Cast Iron, *Scand. J. Metall.*, 1995, **24**, p 48–62
21. M.I. Onsoien, O. Grong, O. Gundersen, and T. Skaland, Process Model for the Microstructure Evolution in Ductile Cast Iron: Part I. The Model, *Metall. Mater. Trans. A*, 1999, **30**, p 1053–1068
22. M.I. Onsoien, O. Grong, O. Gundersen, and T. Skaland, Process Model for the Microstructure Evolution in Ductile Cast Iron: Part II. Applications of the Model, *Metall. Mater. Trans. A*, 1999, **30**, p 1069–1079
23. N. Saunders and A.P. Miodownik, *CALPHAD: Calculation of Phase Diagrams A Comprehensive Guide*. Pergamon, 1998
24. N. Saunders, X. Li, A.P. Miodownik, and J.P. Schille, Modeling of the Thermo-Physical and Physical Properties for Solidification of Al-Alloys, *MS Light Met.*, 2003, p 999–1004
25. D. Raabe, *Computational Materials Science: The Simulation of Materials Microstructure and Properties*. Wiley-VCH, 2002
26. V. Krutiš and J. Roučka, *Shrinkage of Graphitic Cast Irons*. ESI Group Internal Report